Chapter 11
Investigating the Use of Scanning X-Ray Fluorescence to Locate Cryptotephra in Minerogenic Lacustrine Sediment: Experimental Results

Nicholas L. Balascio, Pierre Francus, Raymond S. Bradley, Benjamin B. Schupack, Gifford H. Miller, Bjørn C. Kvisvik, Jostein Bakke and Thorvaldur Thordarson

Abstract Methods to isolate and analyze low concentrations of tephra—*cryptotephra*—are destructive, time consuming, and can be prohibitive when sample size is limited, when looking for tephra over long stratigraphic intervals, or when sediments are minerogenic. Therefore, a more rapid, non-destructive approach to detecting cryptotephra would allow for wider application of tephrochronology and for more complete evaluation of tephra content within sedimentary profiles. In this experiment, we test the ability of scanning X-ray fluorescence to detect tephra glass shards with different composition, concentration, and grain size in minerogenic lacustrine sediment. Synthetic sediment cores spiked with tephra were created in centrifuge tubes, which provided a simple means to introduce tephra in known positions and to replicate the process of analyzing real sediment cores.

N. L. Balascio (✉)
Lamont-Doherty Earth Observatory of Columbia University, Palisades, NY 10964, USA

Department of Geosciences, University of Massachusetts, Amherst, MA 01003, USA
e-mail: balascio@ldeo.columbia.edu

NR. S. Bradley
Department of Geosciences, University of Massachusetts, Amherst, MA 01003, USA

P. Francus
Institut National de la Recherche Scientifique, Centre Eau, Terre et Environnement, Québec, QC G1K 9A9, Canada

GEOTOP, Montréal, QC H3C 3P8, Canada

B. B. Schupack · G. H. Miller
INSTAAR and Department of Geological Sciences, University of Colorado, Boulder, CO 80303, USA

B. C. Kvisvik · J. Bakke
Department of Geography, University of Bergen, Fosswinckelsgate 6, N-5020 Bergen, Norway

T. Thordarson
School of GeoSciences, University of Edinburgh, Edinburgh EH93JW, UK

I. Croudace, G. Rothwell (eds.), *Micro-XRF Studies of Sediment Cores,* Developments in Paleoenvironmental Research, DOI 10.1007/978-94-017-9849-5_11

Book ID: 326999_1_En ChapterID: 11 Dispatch Date: 6/04/2015 ProofNo:1

Background sediment was added incrementally and spun in a centrifuge to create a series of 20 laminations in 4 synthetic cores. Rhyolitic and basaltic tephra were added between laminations with different concentrations and using two grain-size ranges (<53 µm and 105–177 µm). The synthetic cores were split and analyzed on an XRF core scanner, which produced a signal of element composition every 100 µm. Ti, Mn, and Si produced the strongest response to the rhyolitic tephra, and Ti, Mn, Fe, and Cu were most diagnostic of the basaltic tephra. Element ratios were also used to accentuate the difference in composition between tephra and the background sediment. We were able to identify a distinct elemental response across a few cryptotephra horizons, but in general the signal of tephra attenuated quickly with decreasing concentration. Comparison of the signal between different tephra grain size fractions showed that grain size was inversely related to the strength of the elemental response. We also compared these experimental results to XRF scans of a lake sediment core where basaltic and rhyolitic cryptotephra layers had previously been identified using conventional methods. The rhyolitic tephra did not produce a distinct elemental response, but the basaltic tephra was identified in the XRF data. These experiments provide new perspectives on the application and limitations of scanning XRF for cryptotephra studies.

Keywords Tephra · Cryptotephra · Lake sediment · Micro-XRF · Itrax

Introduction

Tephrochronology is a powerful geochronologic tool that can be used to correlate or determine precise ages of a variety of sedimentary archives, including: lake sediments, peat, soils, loess, marine sediments, and glacier ice. Tephra can provide age control in sediments void of material suitable for other dating techniques or supplement existing chronologies. Tephrochronology has a broad range of applications in paleoenvironmental research (Turney and Lowe 2001; Alloway et al. 2007; Lowe 2011). These encompass archaeology (Hall et al. 1994; Newnham et al. 1998; Dugmore et al. 2000; Lowe et al. 2000; Balascio et al. 2011), human evolution (de Menocal and Brown 1999; WoldeGabriel et al. 2005; Deino et al. 2010), the study of landscape change (Manville and Wilson 2004; Dugmore et al. 2009, Streeter et al. 2012), the impact of volcanic eruptions on climate (Zielinski et al. 1994; Zielinski 2000; Gao et al. 2008), and the recurrence interval and hazard assessment of volcanic activity (Newnham et al. 1999; Palumbo 1999; Shane and Hoverd 2002; Wulf et al. 2004; de Fontaine et al. 2007; Molloy et al. 2009).

Recent advances have expanded the potential for using tephrochronology in environments far from volcanic source regions. These regions receive fallout from volcanic eruptions, but in very low concentrations so tephra layers are not visible to the naked eye in sedimentary profiles and are defined as *crypto*tephra layers (Lowe and Hunt 2001; Alloway et al. 2007). It should be noted that *cryptotephra* is an all encompassing term for tephra layers not visible in sedimentary profiles and can refer to a large range of shard concentrations, from single grains to thousands of grains per cm^3, depending on the depositional environment and the distance from the source volcano. Improved techniques for extracting and geochemically analyzing tephra have made possible the use of cryptotephra horizons in paleoenvironmental research (Dugmore et al. 1995; Turney 1998; Hall and Pilcher 2002; Blockley et al. 2005). However, isolating cryptotephra from the background sediment requires detailed laboratory techniques. Generally, samples undergo ashing or acid digestion to remove organic matter. For organic-rich sediments such as peat, these steps are often enough to concentrate tephra. In more minerogenic sediments, fine sieving and multiple density separations are also performed. Samples are then mounted on slides and scanned using a polarized light microscope to identify tephra grains. These methods are destructive and time consuming, and can be prohibitive when sample size is limited, when looking for tephra over broad stratigraphic zones where little or no other age control is available, or when sediments are dominantly minerogenic. Therefore, a more rapid, non-destructive approach to detecting cryptotephra would allow tephrochronology to be applied in more investigations and allow for more complete evaluation of tephra content within sedimentary profiles in order to improve chronologies.

A range of alternative approaches have been attempted, all of which try to exploit unique properties of tephra that are distinguishable from the surrounding sediment. Gehrels et al. (2008) reviewed several non-destructive approaches for detecting tephra in peat cores including: spectrophotometry, x-radiography, magnetic susceptibility, and X-ray fluorescence (XRF). Others have tried to use magnetic properties (Peters et al. 2010), X-ray diffraction (Andrews et al. 2006), and instrumental neutron activation analysis (Lim et al. 2008). De Vleeschouwer et al. (2008) applied petrography, scanning electron microscopy, and scanning XRF to resin-impregnated peat columns. Kylander et al. (2012) examined XRF scans of highly organic-rich sediment cores.

As part of the *Volcanism in the Arctic System (VAST)* project, teams at the University of Massachusetts and the University of Colorado investigated the use of scanning XRF to locate cryptotephra within lacustrine sediment. Scanning XRF uses an intense micro-X-ray beam to analyze the surface of sediment profiles at sub-millimeter resolution and identifies a range of relative elemental components (Croudace et al. 2006). It has been applied in paleolimnology as a rapid and non-destructed approach to characterizing sediment cores. We designed a laboratory-based experiment to test if tephra-bearing sedimentary layers produce a detectable geochemical signature with scanning XRF. In particular, we examine the ability of scanning XRF to locate cryptotephra within minerogenic sediments. Minerogenic sediments are typical in lacustrine environments and are more challenging to date because they often lack enough material for radiocarbon dating, making them ideal targets for tephrochronology. In the laboratory, we created synthetic sediment cores, spiked them with tephra glass shards, and analyzed them on an XRF core scanner. We examined how different tephra concentrations, compositions, and grain sizes are expressed in the scanning XRF elemental data. We also applied this approach to a sediment core from a lake in northern Norway, Sverigedalsvatn, where two cryptotephra layers have been identified using conventional approaches, to test the applicability of our experimental results to an actual sediment profile.

Methods

Experimental Design

Synthetic sediment cores were made in 50 ml centrifuge tubes (Fig. 11.1). We used surface sediment from a glacially fed lake, Lake Tuborg, as the background material. Lake Tuborg is located on Ellesmere Island adjacent to the Agassiz Ice Cap (Smith et al. 2004; Lewis 2009). Sediment input is from snowmelt and glacially fed streams (Lewis et al. 2005, 2007, 2009). The upper sediments are generally in the silt size range (9–17 µm) with some lenses of fine sand (Lewis et al. 2009). We used sediment from this lake because it is almost entirely minerogenic. In addition, Ellesmere Island is located far from volcanic centers so it is unlikely that Lake Tuborg contains tephra in high concentrations.

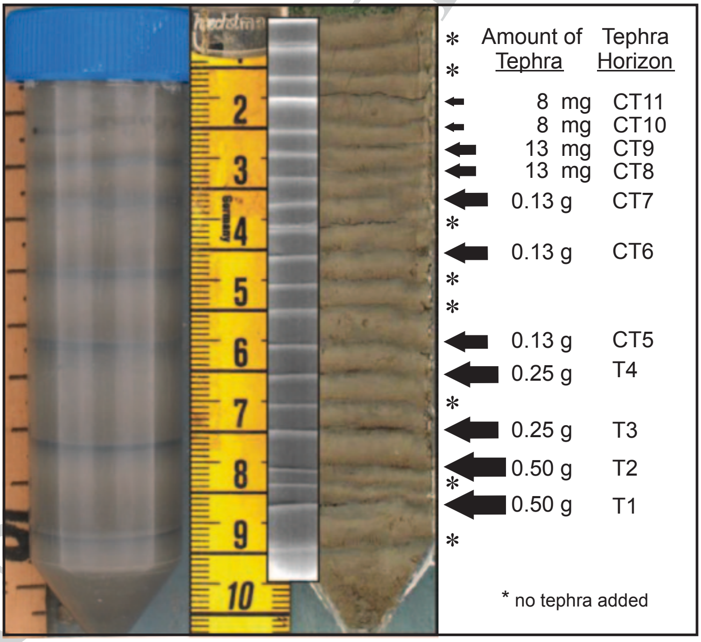

Fig. 11.1 Synthetic sediment cores created in 50 ml centrifuge tubes (*left*). Sediment was added and spun in a horizontal-rotor centrifuge to create multiple fining upward laminations visible in the split cores and in the X-radiographs of the cores (*center*). Between some laminations, tephra was added in different concentrations to form 11 tephra layers, four as visible layers (T1–T4) and seven as cryptotephra layers (CT5–CT11) (*right*)

Book ID: 326999_1_En ChapterID: 11 Dispatch Date: 6/04/2015 ProofNo:1

Sediment from a surface core was homogenized in deionized water, pipetted into centrifuge tubes, and spun in a horizontal-rotor centrifuge to create distinct, fining upward laminations (Fig. 11.1). We made four synthetic sediment cores (R1, R2, B1, B2) with 20, ~0.5 cm-thick laminations (Table 11.1). Tephra was added between some of the laminations and spun in the centrifuge to create discrete layers (Fig. 11.1).

We created 11 tephra layers, T1–T4 and CT5–CT11. Cores R1 and R2 were spiked with a rhyolitic tephra sample from the Icelandic eruption of Askja in 1875 (Sigvaldason 2002; Meara 2011) and cores B1 and B2 were spiked with a basaltic tephra sample from the Icelandic eruption of Grímsvötn in 2004 (Jude-Eton et al. 2012) (Tables 11.1 and 11.2). Both tephra samples were first sieved and cores R1 and B1 only contain tephra <53 µm and cores R2 and B2 only contain tephra between 105 and 177 µm (Table 11.1). All four cores were made simultaneously so the number of laminations, their approximate thickness, and the position where tephra was added are similar.

Tephra was added in successively smaller amounts from the bottom of each core to the top. We started by adding 0.5 g of tephra, which created a ~0.5 mm-thick visible tephra layer, and then progressively reduced the amount of tephra with the smallest amount being 8 mg (Fig. 11.1). By volume, tephra ranged from 100% of the sediment per 0.5-mm section of the core down to 13%. Tephra layers T1–T4 are visible in the split cores and tephra layers CT5–CT11 are cryptic. The visible tephra layers allowed us to identify the elements with the greatest response to tephra within each core. Between some laminations no tephra was added so we could define the background variations. This method of tephra dispersal allowed us to identify the precise locations of each layer and to focus on elemental data across these intervals. However, it does not exactly replicate how most cryptotephra layers are deposited in natural environments, where slower rates of deposition, bioturbation, and landscape reworking often occur causing tephra to be more uniformly incorporated into background sediment and to span broader depth intervals within sediment sequences. For this reason, the amount of tephra added to these synthetic cores may not be directly comparable to tephra concentrations from some cryptotephra studies.

Cores were split, photographed, and analyzed on an Itrax™ XRF core scanner at the University of Quebec's Institut National de la Recherche Scientifique, Centre Eau, Terre et Environnement with a first generation detector. The Itrax™ scans the surface of each core with a 22 mm × 100 µm beam. A range of elements from Al to Zr were detected and output as peak areas reflecting their relative concentration in the sediment. All of the split cores were scanned at 100-µm intervals using an exposure time of 20 s, voltage of 40 kV, and current of 45 mA. We focused our analysis

Table 11.1 Name of synthetic cores, the sample and grains size range of tephra glass shards added to each core

Synthetic core	Tephra	Grain size (µm)
R1	Askja 1875	<53
R2	Askja 1875	105–177
B1	Grímsvötn 2004	<53
B2	Grímsvötn 2004	105–177

Book ID: 326999_1_En ChapterID: 11 Dispatch Date: 6/04/2015 ProofNo:1

Table 11.2 Major element compositions of the synthetic core sediment, tephra used in synthetic cores, and tephra isolated from Sverigedalsvatn

Core	Tephra	–	SiO_2	TiO_2	Al_2O_3	FeO	MnO	MgO	CaO	Na_2O	K_2O	P_2O_5	Total	*n*	Source
Synthetic core sediment	–	–	53.63	0.68	13.82	5.14	0.05	5.69	16.71	0.65	3.50	0.14	100.0	–	This study
Synthetic core B1 & B2	Grims-votn	Mean	50.11	2.81	13.38	13.48	0.23	5.31	9.75	2.65	0.49	0.28	98.47	–	Jude-Eton et al. (2012)
–	2004	1 σ	0.16	0.04	0.16	0.14	0.00	0.07	0.10	0.03	0.01	0.01	0.29	–	–
Synthetic core R1 & R2	Askja 1875	Mean	72.71	0.69	12.52	3.80	0.14	0.91	2.43	4.23	2.19	0.29	99.91	35	Meara (2011)
–	–	1 σ	0.42	0.01	0.12	0.12	0.05	0.04	0.03	0.10	0.02	0.06	0.32	–	–
Sverigedalsvatn	246–247 cm	Mean	49.68	2.97	13.14	13.91	0.25	5.58	10.06	2.56	0.42	0.37	98.93	25	This study
–	–	1 σ	0.46	0.18	0.29	0.43	0.04	0.29	0.30	0.31	0.04	0.05	0.73	–	–
Sverigedalsvatn	283–284 cm	Mean	70.61	0.31	13.70	3.84	0.16	0.21	1.39	4.15	3.31	0.08	97.76	21	This study
–	–	1 σ	1.13	0.06	0.28	0.20	0.04	0.05	0.10	0.71	0.10	0.03	1.34	–	–

on the following elements: Al, Si, Cl, K, Ca, Ti, V, Cr, Mn, Fe, Ni, Cu, Zn, Rb, Sr, and Zr. To avoid effects of the sediment matrix on the XRF signal, element peak areas were divided by the total counts per spectrum.

Application: Sverigedalsvatn Core SVP-207

We compared the scanning XRF signal across tephra layers in the synthetic cores to XRF scans of a sediment core from Sverigedalsvatn (69°12.91′N; 16°02.60′E), a lake in northern Norway, where two Icelandic cryptotephra layers have been identified. A 4.5 m core was recovered from the lake, but we focus our analysis on a section of the core between 230 and 300 cm. The sediment composition is characterized by magnetic susceptibility that was measured every 0.2 cm using a Bartington MS2E meter and by organic matter content measured by loss-on-ignition every 0.5 cm.

Tephra samples were taken at 1-cm intervals from 245–247 cm and 283–287 cm, where tephra from specific Icelandic eruptions were suspected to be located based on a radiocarbon chronology. Samples were processed using conventional approaches to isolate volcanic glass shards (Turney 1998; Hall and Pilcher 2002). Samples were acidified, sieved to isolate grains between 20 and 63 μm, and then subject to heavy-liquid density separations with sodium polytungstate to isolate grains between 2.3 and 2.5 g cm^{-1}. Samples were mounted in epoxy resin and tephra particles were counted using a light microscope. Two significant peaks in tephra concentration were found at 246–247 cm and 283–284 cm where more than 500 shards were observed. Electron microprobe analysis of tephra grains from these samples shows that the lower horizon is a rhyolitic tephra and the upper horizon is a basaltic tephra (Table 11.2). Itrax™ core scans of the entire section were performed at the University of Bergen, Department of Earth Science. The core was scanned at a 200 μm interval using an exposure time of 10 s, voltage of 30 kV, and current of 55 mA.

Results

Background Elemental Variations

There are significant variations in the scanning XRF element profiles of all four synthetic cores that are driven by the physical characteristics of the background sediment and not associated with the presence of tephra (Fig. 11.2). These features are related to the repeated fining-upward sequences within each lamination that was formed during centrifuging. K, Rb, Fe, Ca, and Sr exhibit the strongest variations across each lamination (Fig. 11.2). K, Fe, and Rb increase in value from the base to the top of each lamination, while Ca and Sr decrease across each lamination

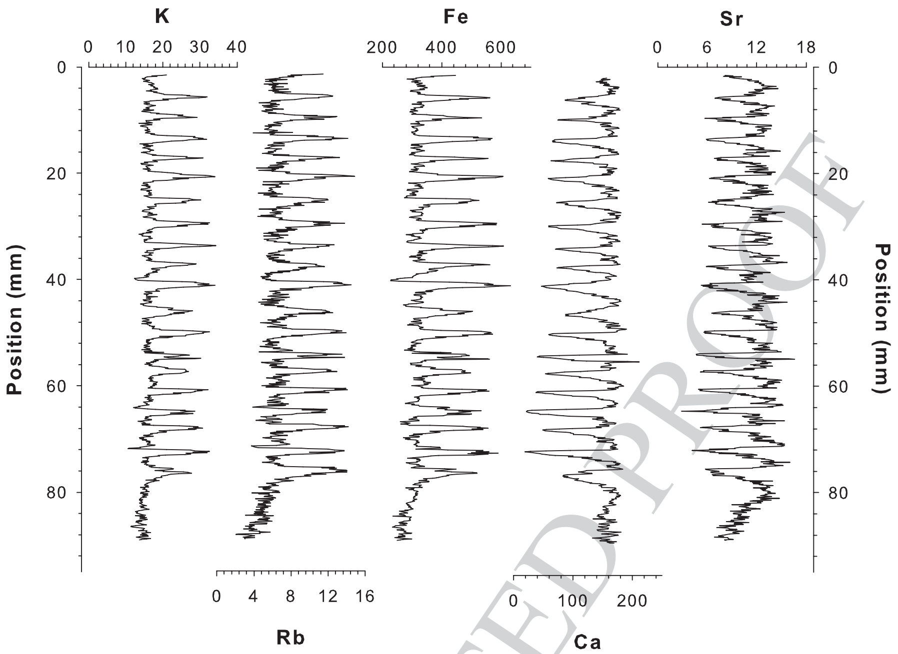

Fig. 11.2 Example from core R1 of the background elemental response present in all of the synthetic cores from fining-upwards of grain size within individual laminations. K, Rb, Fe, Ca, and Sr show the most significant variations across each lamination. Values for each element are presented as peak areas divided by the total counts per spectrum $\times 10^2$

(Fig. 11.2). Principal component analyses of the element matrix for each synthetic core demonstrate the strength of this signal (Table 11.3). The first principal components account for 37–40 % of the variation and are mainly controlled by K, Ca, Fe, Zn, and Rb, which all have factor loadings greater than 0.8 or less than −0.8. These data establish the background XRF signal and help guide how the elemental data are analyzed for the presence of tephra.

Synthetic Cores Spiked with Rhyolitic Tephra (R1 and R2)

Eleven rhyolitic tephra layers were added between laminations within cores R1 and R2 with grain size ranges of <53 μm and 105–177 μm, respectively (Figs. 11.3 and 11.4). In core R1, single element profiles of Ti, Mn, and Si show the strongest responses across the visible tephra layers (Fig. 11.3). Mn values have the most well defined peaks and clearly identify tephra layers T1, T2, T3, and T4 (Fig. 11.3). The peaks in Mn are larger across T1 and T2 than across T3 and T4. There is a small peak at cryptotephra layer CT6, but it is not as distinct and barely above background values. There is no clear signal in the Mn values of tephra layers with lower concentrations, CT7–CT11. Ti and Si also show slight increases at the positions of T1, T2, and T4.

Table 11.3 Principal component analysis results for scanning XRF elemental data for each synthetic core. Data are from the first principle component. Factor loadings greater than 0.8 are in bold

Synthetic core	R1	R2	B1	B2
Eigenvalue	6.573	6.309	6.517	6.670
% Variability	41.084	39.430	40.733	41.689
Factor loadings				
Al	0.229	0.281	0.374	0.375
Si	-0.450	-0.411	-0.421	-0.468
Cl	0.014	0.000	-0.073	-0.051
K	*0.930*	*0.936*	0.766	*0.927*
Ca	*-0.836*	*-0.820*	*-0.872*	*-0.833*
Ti	0.585	0.673	0.622	0.626
V	0.382	0.366	0.543	0.489
Cr	0.432	0.290	0.359	0.426
Mn	0.305	0.461	0.507	0.380
Fe	*0.965*	*0.958*	*0.918*	*0.956*
Ni	0.707	0.676	0.770	0.697
Cu	0.731	0.760	*0.814*	0.721
Zn	*0.859*	*0.856*	*0.879*	*0.840*
Rb	*0.858*	0.791	0.668	*0.831*
Sr	-0.737	-0.555	-0.631	-0.691
Zr	-0.057	0.100	-0.256	-0.064

Profiles of Ti, Mn, and Si relative to Ca exhibit the most distinct peaks across these tephra layers as compared with the single element profiles (Fig. 11.3). Ca responds strongly to changes in grain size associated with the artificial laminations.

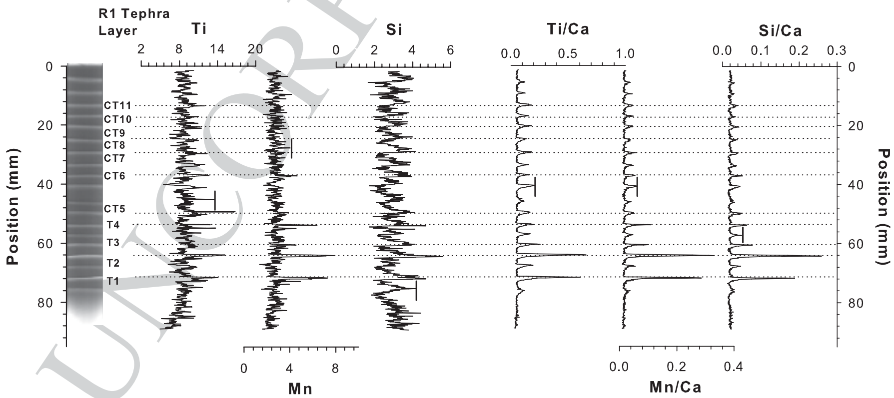

Fig. 11.3 Scanning XRF data and X-radiograph for synthetic core R1, which was spiked with rhyolitic tephra less than 53 µm. Values for each element are presented as peak areas divided by the total counts per spectrum $\times 10^2$. The highest background value is marked on each plot with a vertical bar. Tephra (T) and cryptotephra (CT) layers interpreted to have element peaks above background variations that indicate their presence in the sediment are underlined

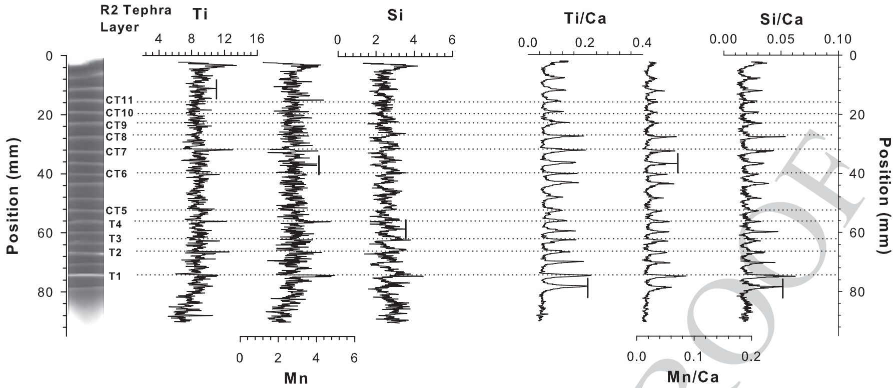

Fig. 11.4 Scanning XRF data and X-radiograph for synthetic core R2, which was spiked with rhyolitic tephra from 105 to 177 µm. Values for each element are presented as peak areas divided by the total counts per spectrum × 10^2. The highest background value is marked on each plot with a vertical bar. Tephra (T) and cryptotephra (CT) layers interpreted to have element peaks above background variations that indicate their presence in the sediment are underlined

Ca values decrease across the laminations while Ti, Mn, and Si values increase. These trends are expressed as the slight increases the element ratios that mark the top of each blank lamination. Peaks in these element ratios that are above these background variations occur at T1, T2, and T3 for Ti/Ca, Mn/Ca, and Si/Ca. Mn/Ca and Si/Ca values also show a response above background levels at T4, but none of the ratios indicate the presence of the cryptotephra layers (CT5–CT11).

In core R2, we also examined the response of Ti, Mn, and Si at each tephra layer (Fig. 11.4). Overall, the elemental response across the tephra layers is less pronounced. Si values show no clear signature of tephra at any position in the core. The Mn profile only shows a small peak above the background level at T1 and T4. Ti has peaks at T2, T4, and CT7 that are above the background, but show no variation in peak height that correspond with tephra concentration and do not seem to reliably represent the presence of tephra. Ratios of Ti, Mn, and Si to Ca only show a distinct response at T1 and the response across the other tephra layers are below the background variations.

Synthetic Cores Spiked with Basaltic Tephra (B1 and B2)

Eleven basaltic tephra layers were added between laminations within cores B1 and B2 with grain size ranges of < 53 µm and 105–177 µm, respectively (Figs. 11.5 and 11.6). In core B1, single element profiles of Ti, Mn, Fe and Cu show the strongest responses across the tephra layers and indicate the presence of three of the cryptotephra layers (Fig. 11.5). A sharp increase in values for Ti, Mn, and Fe is clearly distinguishable from background variations across tephra layers T1–T4 and CT5. Cu values show clear peaks at T1–T4. Peaks that exceed background values are also present in the profiles of Mn across CT6, and Ti across CT6 and CT8. In general, the peak heights generally decrease with decreasing concentration of tephra.

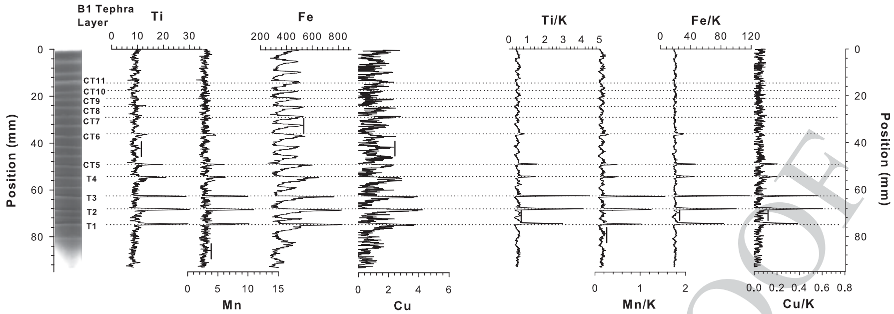

Fig. 11.5 Scanning XRF data and X-radiograph for synthetic core B1, which was spiked with basaltic tephra less than 53 µm. Values for each element are presented as peak areas divided by the total counts per spectrum × 10^2. The highest background value is marked on each plot with a vertical bar. Tephra (T) and cryptotephra (CT) layers interpreted to have element peaks above background variations that indicate their presence in the sediment are underlined

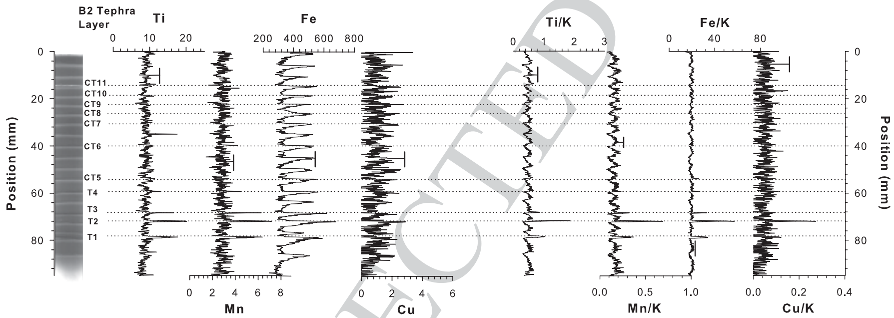

Fig. 11.6 Scanning XRF data and X-radiograph for synthetic core B2, which was spiked with basaltic tephra from 105 to 177 µm. Values for each element are presented as peak areas divided by the total counts per spectrum × 10^2. The highest background value is marked on each plot with a vertical bar. Tephra (T) and cryptotephra (CT) layers interpreted to have element peaks above background variations that indicate their presence in the sediment are underlined

The ratios of Ti, Mn, Fe, and Cu to K produce the most significant response across the basaltic tephra layers of core B1 (Fig. 11.5). K responds strongly to changes in grain size associated with the artificial laminations. K values increase across the laminations relative to Ti, Mn, Fe, and Cu. These trends are expressed as the slight decreases in the element ratios that mark the top of each blank lamination. Profiles of Ti/K, Mn/K, Fe/K, and Cu/K have sharp peaks at the tephra layers that are much greater than the background values. All four profiles show strong responses across the first five tephra layers. Plots of Ti/K and Fe/K also show peaks above background values across CT6. The response across tephra layers T1–T3 is greater than across T4–CT6.

In core B2, we also examined the response of Ti, Mn, Fe, and Cu (Fig. 11.6). The single element profile of Mn has the most distinct peaks. Significant increases in Mn values occur across tephra layers T1–T3 and there are peaks just above the background values at T4 and CT6, but overall the response is not as strong as in core B1. There are no peaks in Cu that indicate the presence of any of the tephra layers. The Ti and Fe profiles show slight increases at T1, T2, and T3, but lack clear evidence for the presence of any of the other tephra layers. Although Ti has peaks across T1–T3, there is a high background spike between CT6 and CT7 that is of similar height as at T1 and T3. This peak is only composed of a single data point and may be an aberrant value due to matrix effects or is possibly the signal of a small concentration of tephra that was introduced mistakenly during construction of the cores.

The ratio of Ti, Mn, Fe, and Cu to K in core B2 show distinct peaks and have low background variations (Fig. 11.6). Profiles of Ti/K, Mn/K, and Fe/K show distinct peaks at T1–T3 and Fe/K values also increase at T4 and CT5. These element ratio profiles more clearly define these tephra horizons compared to the single element plots. The Cu/K ratio only displays a significant peak at T2.

Sverigedalsvatn Core SVP-207

Two cryptotephra horizons were identified in Sverigedalsvatn with peaks in concentration greater than 500 shards per cm^3 occurring at 246–247 cm and 283–284 cm (Fig. 11.7). The lower tephra horizon is rhyolitic and has a high SiO_2 (70.61 %) and low FeO (3.84 %) content and the upper tephra horizon is basaltic and has a lower

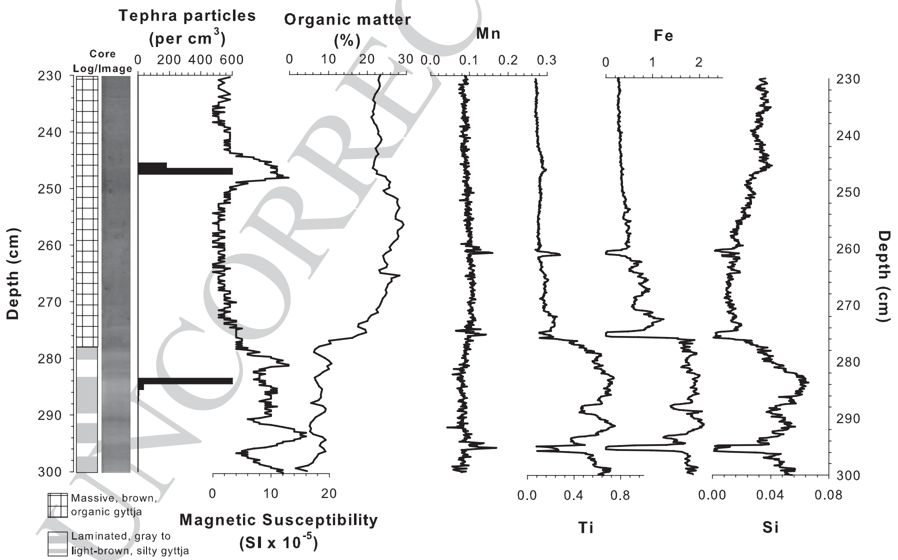

Fig. 11.7 Section of the Sverigedalsvatn core where two cryptotephra layers were identified. The concentrations of tephra are compared to magnetic susceptibility and organic matter content profiles, which show significant changes in sediment composition, and scanning XRF profiles of Mn, Ti, Fe, and Si. Values for each element are presented as peak areas divided by the total counts per spectrum. Graphic log and core image are also shown

Book ID: 326999_1_En ChapterID: 11 Dispatch Date: 6/04/2015 ProofNo:1

SiO_2 (49.68 %) and higher FeO (13.91 %) content, which are similar in composition to the two tephra used in making the synthetic cores (Table 11.2).

The section of the core from Sverigedalsvatn (230–300 cm), where the two cryptotephra horizons were found, contains significant compositional changes, reflected in organic matter content and magnetic susceptibility profiles (Fig. 11.7). The lower sediments, from 278 to 300 cm, are minerogenic with high magnetic susceptibility values and low organic content. There is a transition to more organic-rich sediment above 278 cm, where magnetic susceptibility decreases and organic matter values increase to an average of 24 %. There is an increase in magnetic susceptibility from 244 to –250 cm at the location where the upper tephra was identified.

Element profiles that were most diagnostic of tephra in the synthetic core experiment were examined in Sverigedalsvatn. Ti, Fe, and Si profiles across the entire core section show a response to the major compositional changes (Fig. 11.7). Values for these elements are highest from 278–300 cm, sharply decrease at 278 cm, and are low from 278 to 230 cm. These trends are similar to changes in magnetic susceptibility and are opposite the trend in organic content. Mn was also diagnostic of tephra in the synthetic core experiment, but varies independently with relatively constant high frequency, low amplitude fluctuations.

Across the rhyolitic tephra horizon, elemental values around 283–284 cm show no clear departures from the background (Fig. 11.8). There are slight increases in Si, Ti/Ca, and Si/Ca around this depth, but the changes in values are probably associated with other physical properties of the sediment. At the upper tephra horizon, elemental values immediately around 246–247 cm show a response that is likely related to the presence of tephra (Fig. 11.8). Ti values sharply increase and then slowly decline. Ti/K values exhibit a similar, but slightly more distinct trend. At both locations we also examined the response of other elements, but did not find any that showed a more significant response.

Discussion

Scans of tephra-spiked synthetic cores provide a better perspective on the XRF response to tephra composition, concentration, and grain size and how analysis of the data can be approached. There are a variety of background sediments and tephra that could have been used, but these experiments specifically target scenarios in lacustrine environments where sediments have variable grain sizes and are dominantly minerogenic.

Elemental Signal of Tephra in Synthetic Cores

For each core we used single element profiles to examine elements with the strongest response across the tephra layers as compared to background levels, which we defined as the range of values for a given element across the laminations where

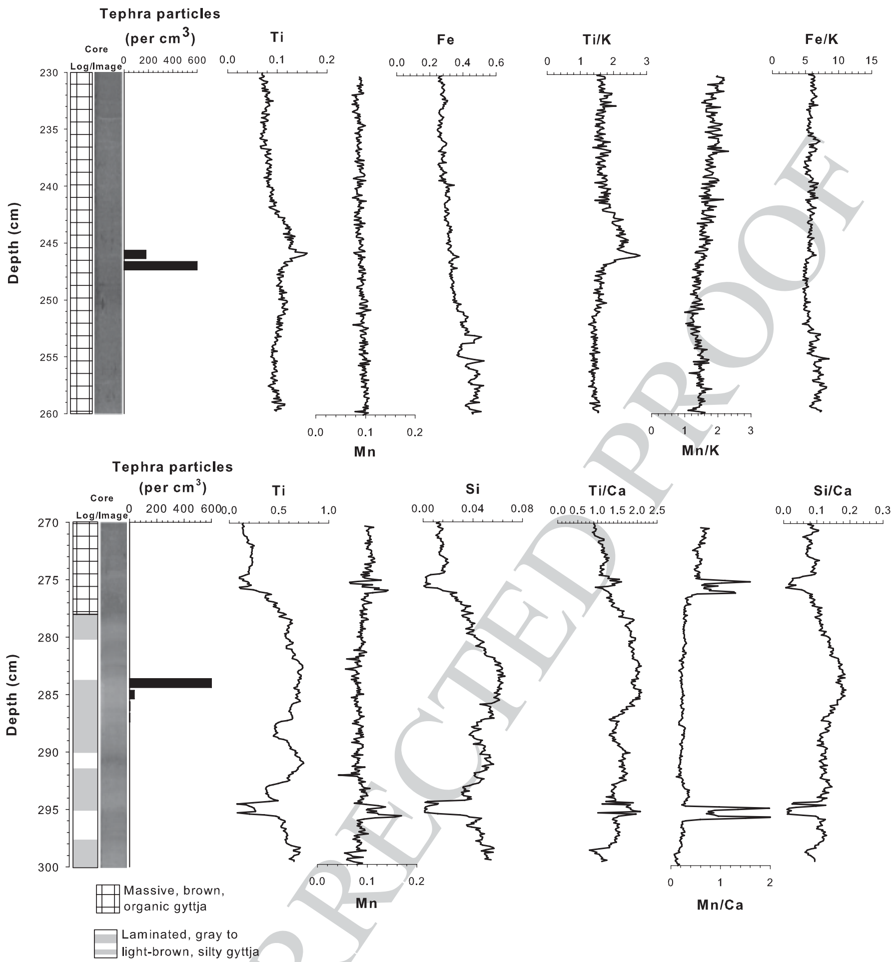

Fig. 11.8 Expanded views of the sections of the Sverigedalsvatn core where the basaltic cryptotephra layer was identified (*upper panel*) and where the rhyolitic cryptotephra layer was identified (*lower panel*). The location of the basaltic tephra is compared to scanning XRF profiles of Ti, Mn, Fe, Ti/K, Mn/K, and Fe/K. The location of the rhyolitic tephra is compared to scanning XRF profiles of Ti, Mn, Si, Ti/Ca, Mn/Ca, and Si/Ca. Values for each element are presented as peak areas divided by the total counts per spectrum. Graphic log and core image are also shown

no tephra was added. Visible tephra layers, T1–T4, produce the strongest response and show which elements should be examined to try and locate cryptotephra layers, CT5–CT11. We also use element ratios, which show a greater response across tephra layers and more clearly define deviations from background elemental variations. We present the elements identified as most diagnostic of tephra relative to Ca and K for the cores spiked with rhyolitic and basaltic tephra, respectively, which are the element ratios that showed the greatest difference between tephra layers and the background variations. We were not able to detect all 11 tephra layers in any of the four synthetic cores, but we were able to characterize conditions where the elemental response to tephra is greatest and we were able to identify a significant response to a few of the cryptotephra layers.

First, we consider the relative signature of the four visible tephra layers (T1–T4) to better understand how tephra grain size and composition are detected by scanning XRF. The different tephra compositions (rhyolitic and basaltic) had slightly different diagnostic elements and relative responses. Synthetic sediment cores spiked with rhyolitic tephra show that Ti, Mn, and Si produced the strongest response to tephra, while Ti, Mn, Fe, and Cu are most diagnostic of the presence of the basaltic tephra. These results are a function of the compositional differences between rhyolitic and basaltic tephra (Table 11.1), as well as the relative difference between the composition of the tephra and the background sediment. Comparison between the relative response across tephra layers in the 'B' cores and the 'R' cores shows that the basaltic tephra layers in B1 and B2 produce the more distinct element peaks and at lower concentrations than the rhyolitic tephra layers in cores R1 and R2. Both of these properties reflect the greater compositional difference between the basaltic tephra and the background sediment as compared to the rhyolitic tephra. Similar results were found by Kylander et al. (2012) in their analysis of the response of basaltic and rhyolitic tephra in organic-rich sediment cores.

Tephra grain size was found to affect the elemental response across both basaltic and rhyolitic tephra layers. Cores R1 and B1, spiked with tephra <53 μm, had greater elemental responses compared to cores R2 and B2, spiked with tephra 105–177 μm. There are no compositional variations of the tephra with grain size that would cause this response and this trend is likely the result of difference in grain packing and density. The XRF response is greater across finer grained layers, which have a tighter packing and greater surface area per volume that interacts with the X-rays and causes a stronger response.

We found that the elemental response is directly related to tephra concentration. The visible tephra layers, T1 and T2 generally had a greater response than T3 and T4, where less tephra was added. However, most cryptotephra layers (CT5–CT11) were undistinguishable from the background sediment. The most cryptotephra layers were observed in core B1, where fine grained basaltic tephra, even in extremely low concentrations, was able to affect the bulk geochemical composition and produce an elemental peak above background values.

We analyzed both single element and element ratio profiles across the synthetic cores. Element ratios exhibited greater differences between tephra layers and the background sediment. For these tephra and background sediment compositions, elements relative to Ca provided optimum detection in cores R1 and R2, and elements relative to K in cores B1 and B2. This occurs because Ca and K are the elements with the greatest difference in concentration between the background sediment and the rhyolitic and basaltic tephra, respectively (Table 11.2). Ca and K do also respond differently to the fining-upwards of grain size associated with each lamination, however the compositional difference of these two tephras had greater control on the element ratio than this background signal.

Elemental Signal of Tephra in Sverigedalsvatn Core SVP-207

XRF scans of Sverigedalsvatn core SVP-207 provide a comparison of the elemental signal of cryptotephra in an actual sediment core to results from the synthetic core experiment. Scans of SVP-207 show a distinct signal of the basaltic tephra (Figs. 11.7, 11.8). This cryptotephra layer is associated with an increase in Ti and Ti/K values, but no other significant elemental response and no clear indication of the rhyolitic tephra was observed. The detection of the basaltic tephra shows a similar result as with the synthetic core experiment and is an expected trend since there is a greater difference between the composition of basaltic tephra and typical siliciclastic sediment.

This application also demonstrates the complicating factors that large changes in sedimentology have on detecting tephra with scanning XRF. In Sverigedalsvatn, there are significant changes in sedimentology and element values across this section of the core (Fig. 11.7). The elemental response to the basaltic cryptotephra layer is much less than the elemental response to changes in lithology associated with natural environmental conditions (minerogenic versus organic) and incidental events such as the unexplained Ti peak around 265 cm depth (Fig. 11.7). The core from Sverigedalsvatn was scanned using slightly different analytical conditions, including shorter counting times, which does complicate direct comparison.

Application and Limitations of Scanning XRF to Locate Cryptotephra in Sediment Profiles

Here we present a systematic approach to exploring the use of scanning XRF to locate cryptotephra in sediment profiles, which allows us to assess the application and limitations of the method. We were able to identify a few cryptotephra horizons in this study. The elements and element ratios we found diagnostic of tephra can be applied in looking for tephra in natural sediment profiles, although these may vary depending on the specific tephra being targeted and the background sediment composition. The success of this method is also likely to be greater where the background element variations are minimal, where there are large differences in geochemistry between tephra and the background sediment, and where tephra is in a high enough concentration to affect the bulk geochemical composition of the sediment.

Despite these positive results, many of the cryptotephra layers in this study did not produce a distinct elemental response highlighting some of the difficulty in applying this method. Our laboratory experiment allowed for idealized sedimentary conditions. Specifically, the synthetic cores had a consistent background signal throughout, which is not the case in most sediment profiles where minor changes in sedimentology can result in large changes in the background XRF signal that can obscure a cryptotephra layer. In addition, we dispersed tephra as discrete layers between laminations, which allowed us to identify precise locations where tephra was located, but this is not representative of how tephra is naturally deposited. Another complicating factor that may have affected this experiment is the XRF counting time (20 s) that we chose to use in analyzing all of the synthetic cores. By increasing the counting time we might have been able to show a more distinct response across some of the lower concentration tephra layers and may have increased detection of the lighter elements, specifically Al. Al_2O_3 is typically the second most abundant oxide in both basaltic and rhyolitic tephra and could be a diagnostic element, assuming there is a significant difference between its concentration and the background sediment.

These results provide a first step in establishing protocols for the analysis of cryptotephra by scanning XRF. Further work could include improvements to this experimental design, including: varying how tephra are dispersed within the sediment matrix, using a range of background sediment types without strong grain-size effects, using of a wider range of tephra compositions, and examining the effects of varying counting times. Moreover, the new generation of scanners come with detectors with lower detection limits, especially for light elements and would allow for the use of Al as a normalizer, hence an easier comparison with the results obtained by the tephra community with classical analysis techniques.

Conclusions

Tephra-spiked synthetic cores were created and analyzed on an XRF core scanner to examine the elemental signal of tephra with different compositions, concentrations, and grain size within a matrix of minerogenic lacustrine sediment. We were able to identify elements and element ratios diagnostic of basaltic and rhyolitic tephra. Synthetic sediment cores spiked with rhyolitic tephra showed that Ti, Mn, and Si produced the strongest response to tephra, while Ti, Mn, Fe, and Cu were most diagnostic of the presence of the basaltic tephra. The ratio of these diagnostic elements of tephra relative to Ca and K for the cores spiked with rhyolitic and basaltic tephra, respectively, showed the greatest difference between tephra layers and the background variations. We were not able to detect all of the tephra layers in any of the four synthetic cores, but we were able to characterize conditions where the elemental response to tephra is greatest and we were able to identify a significant response to a few of the cryptotephra layers. Our results also showed that finer grained tephra produced a larger elemental response. XRF scans of the synthetic cores were also compared to scans of an actual sediment profile, known to contain a basaltic and a rhyolitic cryptotephra to demonstrate how our controlled laboratory experiment might be applied. In addition to exploring the utility of scanning XRF to locating tephra in sedimentary sequences, the analytical approaches used in this experiment can be helpful for other studies examining discrete or exotic grains within a sedimentary matrix.

Acknowledgements This project was funded by National Science Foundation grant ARC-0714074, and by a NSERC discovery grant to PF. Support was also provided by a U.S. Fulbright Program Fellowship awarded to NLB, and analysis of the core from Lake Sverigedalsvatn was part of the ARCTREC project supported by the Norwegian Research Council. We would like to thank members of the VAST project team for helpful discussions, Ted Lewis for providing us with surface sediment from Lake Tuborg, and two anonymous reviewers for their comments on an earlier draft.

References

Alloway BV, Larsen G, Lowe DJ, Shane PAR, Westgate JA (2007) Tephrochronology. In: Elias SA (ed) Encyclopaedia of quaternary science. Elsevier, Oxford, pp 2869–2898

Andrews JT, Eberl DD, Kristjansdottir GB (2006) An exploratory method to detect tephras from quantitative XRD scans: examples from Iceland and East Greenland marine sediments. Holocene 16:1035–1042

Balascio NL, Wickler S, Narmo LE, Bradley RS (2011) Distal cryptotephra found in a Viking boathouse: the potential for tephrochronology in reconstructing the Iron Age in Norway. J Archaeol Sci 38:934–941

Blockley SPE, Pyne-O'Donnell SDF, Lowe JJ, Mathews IP, Stone A, Pollard AM, Turney CSM, Molyneux EG (2005) A new and less destructive laboratory procedure for the physical separation of distal glass tephra shards from sediments. Quat Sci Rev 24:1952–1960

Croudace IW, Rindby A, Rothwell RG (2006) ITRAX: description and evaluation of a new multi-function X-ray core scanner. In: Rothwell RG (ed) New techniques in sediment core analysis, vol 267. Geological Society Special Publication, London, pp 51–564

Deino AL, Scott GR, Saylor B, Alene M, Angelini JD, Haile-Selassie Y (2010) ^{40}Ar/^{39}Ar dating, paleomagnetism, and tephrochemistry of Pliocene strata of the hominid-bearing Woranso-Mille area, west-central Afar Rift, Ethiopia. J Hum Evol 58:111–126

de Menocal PB, Brown FH (1999) Pliocene tephra correlations between East African hominid localities, the Gulf of Aden, and the Arabian Sea. In: Agustí J, Rook L, Andrews P (eds) Hominoid evolution and climatic change in Europe, vol 1. Cambridge University Press, Cambridge, pp 23–54

De Vleeschouwer F, van Vliët-Lanoé B, Fagel N, Richter T, Boës X (2008) Development and application of high-resolution petrography on resin-impregnated Holocene peat columns to detect and analyse tephras, cryptotephras, and other materials. Quat Int 178:54–67

Dugmore AJ, Larsen G, Newton AJ (1995) Seven tephra isochrones in Scotland. Holocene 5:257–266

Dugmore AJ, Newton AJ, Larsen G, Cook GT (2000) Tephrochronology, environmental change, and the Norse settlement of Iceland. Environ Archaeol 5:21–34

Dugmore AJ, Gísladóttir G, Simpson IA, Newton A (2009) Conceptual models of 1200 years of Icelandic soil erosion reconstructed using tephrochronology. J North Atlantic 2:1–18

de Fontaine CS, Kaufman DS, Anderson RS, Werner A, Waythomas CF, Brown TA (2007) Late Quaternary distal tephra-fall deposits in lacustrine sediments, Kenai Peninsula, Alaska. Quat Res 68:64–78

Gao C, Robock A, Ammann C (2008) Volcanic forcing of climate over the past 1500 years: an improved ice core-based index for climate models. J Geophys Res 113:D23111

Gehrels MJ, Newnham RM, Lowe DJ, Wynne S, Hazell ZJ, Caseldine C (2008) Towards rapid assay of cryptotephra in peat cores: review and evaluation of various methods. Quat Int 178:68–84

Hall VA, Pilcher JR (2002) Late Quaternary Icelandic tephras in Ireland and Great Britain: detection, characterization and usefulness. Holocene 12:223–230

Hall VA, Pilcher JR, McVicker SJ (1994) Tephra-linked studies and environmental archaeology, with special reference to Ireland. Circaea 11:17–22

Jude-Eton T, Thordarson T, Gudmundsson MT, Oddsson B (2012) Dynamics, stratigraphy and proximal dispersal of supraglacial tephra during the ice-confined 2004 eruption at Grímsvötn Volcano, Iceland. Bull Volcanol 74:1057–1082

Kylander ME, Lind EM, Wastegård S, Löwemark L (2012) Recommendations for using XRF core scanning as a tool in tephrochronology. Holocene 22:371–375

Lewis T (2009) Normal and extreme sedimentation and physical processes in Lake Tuborg, Ellesmere Island, Nunavut. Ph. D. Thesis. University of Massachusetts Amherst, pp 199

Lewis T, Braun C, Hardy DR, Francus P, Bradley RS (2005) An extreme sediment transfer event in a Canadian high arctic stream. Arct Antarct Alp Res 37:477–482

Lewis T, Francus P, Bradley RS (2007) Limnology, sedimentology, and hydrology of a jökulhlaup into a meromictic high arctic lake. Can J Earth Sci 44:791–806

Lewis T, Francus P, Bradley RS (2009) Recent occurrence of large jökulhlaups at Lake Tuborg, Ellesmere Island, Nunavut. J Paleolimnol 41:491–506

Lim C, Ikehara K, Toyoda K (2008) Cryptotephra detection using high-resolution trace-element analysis of Holocene marine sediments, southwest Japan. Geochim Cosmochim Acta 72:5022–5036

Lowe DJ (2011) Tephrochronology and its application: a review. Quat Geochronol 6:107–153

Lowe DJ, Hunt JB (2001) A summary of terminology used in tephra-related studies. Les Dossiers de l'Archeo-Logis 1:17–22

Lowe DJ, Newnham, RM, McFadgen, BG, Higham, TFG (2000) Tephras and New Zealand archaeology. J Archaeol Sci 27:859–870

Manville V, Wilson CJN (2004) The 26.5 ka Oruanui eruption, New Zealand: a review of the roles of volcanism and climate in the post-eruptive sedimentary response. N Z J Geol Geophys 47:525–547

Meara R (2011) Climatic and environmental impact of Holocene silicic explosive eruptions in Iceland. Ph. D. Thesis. University of Edinburgh, pp 324

Molloy C, Shane P, Augustinus P (2009) Eruption recurrence rates in a basaltic volcanic field based on tephra layers in maar sediments: Implications for hazards in the Auckland volcanic field. Geol Soc Am Bull 121:1666–1677

Newnham RM, Lowe D J, McGlone MS, Wilmshurst JM, Higham TFG (1998) The Kaharoa Tephra as a critical datum for earliest human impact in northern New Zealand. J Archaeol Sci 25:533–544

Newnham RM, Lowe DJ, Alloway BV (1999) Volcanic hazards in Auckland, New Zealand: a preliminary assessment of the threat posed by central North Island silicic volcanism based on the quaternary tephrostratigraphical record. In: Firth CR, McGuire WJ (eds) Volcanoes in the quaternary, vol 161. Geological Society of London Special Publications, London, pp 27–45

Palumbo A (1999) The activity of Vesuvius in the next millennium. J Volcanol Geoth Res 88:125–129

Peters C, Austin WEN, Walden J, Hibbert FD (2010) Magnetic characterization and correlation of a Younger Dryas tephra in North Atlantic marine sediments. J Quat Sci 25:339–347

Shane P, Hoverd J (2002) Distal record of multi-sourced tephra in Onepoto Basin, Auckland, New Zealand: implications for volcanic chronology, frequency and hazards. Bull Volcanol 64:441–454

Sigvaldason GE (2002) Volcanic and tectonic processes coinciding with glaciation and crustal rebound: an early Holocene rhyolitic eruption in the Dyngjufjöll volcanic centre and the formation of the Askja caldera, north Iceland. Bull Volcanol 64:192–205

Smith SV, Bradley RS, Abbott MB (2004) A 300 year record of environmental change from Lake Tuborg, Ellesmere Island, Nunavut, Canada. J Paleolimnol 32:137–148

Streeter R, Dugmore AJ, Vésteinsson, O (2012) Plague and landscape resilience in premodern Iceland. Proc Nat Acad Sci 109:3664–3669

Turney CSM (1998) Extraction of rhyolitic component of Vedde microtephra from minerogenic lake sediments. J Paleolimnol 19:199–206

Turney CSM, Lowe JJ (2001) Tephrochronology. In: Last WM, Smols JP (eds) Tracking environmental change using lake sediments, vol 1: basin analysis, coring, and chronological techniques. Kluwer, Dordrecht, pp 451–471

WoldeGabriel G, Hart W K, Katoh S, Beyene Y, Suwa G (2005) Correlation of Plio-Pleistocene tephra in Ethiopian and Kenyan rift basins: temporal calibration of geological features and hominid fossil records. J Volcanol Geotherm Res 147:81–108

Wulf S, Kraml M, Brauer A, Keller J, Negendank JFW (2004) Tephrochronology of the 100 ka lacustrine sediment record of Lago Grande di Monticchio (southern Italy). Quat Int 122:7–30

Zielinski GA (2000) Use of paleo-records in determining variability within the volcanism-climate system. Quat Sci Rev 19:417–438

Zielinski GA, Mayewski PA, Meeker LD, Whitlow S, Twickler MS, Morrison M, Meese DA, Gow AJ, Alley RB (1994) Record of volcanism since 7000 B.C. from the GISP2 Greenland ice core and implications for the volcano-climate system. Science 264:948–952